Chirality and polarization of inertial antiferromagnetic resonances driven by spin-orbit torques

Peng-Bin He [*]
School of Physics and Electronics, Hunan University, Changsha 410082, China

Ri-Xing Wang
College of Computer and Electrical Engineering, Hunan University of Arts and Science, Changde 415000, China

Zai-Dong Li
Tianjin Key Laboratory of Quantum Optics and Intelligent Photonics, School of Science, Tianjin University of Technology, Tianjin 300384, China and School of Mathematics and Physics, Xinjiang Hetian College, Hetian 848000, China

Mikhail Cherkasskii [†]
Institute for Theoretical Solid State Physics, RWTH Aachen University, DE-52074 Aachen, Germany

(Received 15 July 2025; revised 19 November 2025; accepted 23 November 2025; published 11 December 2025)

It is widely accepted that the handedness of a resonant mode is an intrinsic property. We show that, by tailoring the polarization and handedness of alternating spin-orbit torques used as the driving force, the polarization state and handedness of inertial resonant modes in an antiferromagnet (AFM) can be actively controlled. In contrast with ferromagnets, whose resonant-mode polarization is essentially fixed, AFM inertial modes can continuously evolve from elliptic through circular to linear polarization as the driving polarization is varied. We further identify an inertia-dependent critical degree of driving polarization at which the mode becomes linearly polarized while its handedness reverses.

DOI: 10.1103/1cjr-7cgl

I. INTRODUCTION

Spin inertia [1] in magnetically ordered materials can be induced by various microscopic mechanisms, as demonstrated in recent studies. First-principles spin dynamics have shown that both damping and inertia emerge consistently from the electronic structure, emphasizing the role of spin-orbit coupling in dissipative and inertial spin dynamics [2,3]. A complementary approach based on spin-bath coupling reveals that a non-Markovian memory kernel yields an effective inertial term in the spin equation of motion [4,5]. Additionally, nonadiabatic interactions with environmental degrees of freedom can produce inertialike corrections [6]. A classical interpretation models the spin as a circular current loop, leading to inertial terms from the underlying mechanical dynamics [7,8].

Spin inertia gives rise to magnetic nutation [6,9–12], which manifests as nutation resonance [13–16]. Furthermore, inertia modifies the self-oscillatory dynamics of magnetization in both antiferromagnets (AFMs) [17,18] and ferromagnets (FMs) [19]. The characteristic influence of spin inertia on these uniform magnetic dynamics can serve as an additional experimental probe for its detection.

Apart from experimental observations of nutation [13–16], extensive efforts have been invested in the theoretic research of nutational resonance [20–29]. It was found that the inertial magnetization dynamics are described by the inertial Landau-Lifshitz-Gilbert (ILLG) equation, which predicts a nutation resonance in addition to conventional FM resonance. Olive *et al.* [20,21] numerically demonstrated a secondary high-frequency peak whose amplitude and position depend on the inertial relaxation time, the damping, and the applied field. In subsequent analytical studies, shifts of resonant frequencies and linewidths of both precession and nutation have been quantified, revealing a nontrivial dependence on damping and magnetic anisotropy [22,27–29]. Authors of another analytical study have predicted that these effects are enhanced in AFMs due to exchange interaction [23]. Remarkably, when driven by a circularly polarized magnetic field, FMs exhibit a single nutational peak and a single precessional peak, whereas AFMs and ferrimagnets present these peaks in pairs. In the latter two systems, inter- and intrasublattice couplings further tune these resonances, indicating distinct mechanisms in multisublattice systems [24,26]. Finally, spin pumping at terahertz nutation frequencies produces a spin current opposite in direction to that generated by precessional modes, providing an unambiguous experimental signature of nutation [25].

[*]Contact author: hepengbin@hnu.edu.cn
[†]Contact author: macherkasskii@hotmail.com

Published by the American Physical Society under the terms of the Creative Commons Attribution 4.0 International license. Further distribution of this work must maintain attribution to the author(s) and the published article's title, journal citation, and DOI.

We note that authors of most studies on inertial resonances have primarily focused the resonant frequency, determined by the intrinsic magnetic properties. However, the polarization of the resonant mode, which depends on both the magnetic material and the external drive, remains comparatively unexplored, despite offering an extra degree of freedom—in addition to amplitude and phase—for information encoding [30–33]. Experimentally, resonance is usually driven by circularly or linearly polarized magnetic fields. Accordingly, the nutational resonances in the current theoretical studies were assumed to be excited by circularly [22–26,29] or linearly polarized [20,21] oscillating fields.

An alternative utilizes current-induced spin-torque resonance, realized via spin-transfer torques in spin-valve structures [34–39] and spin-orbit torques (SOTs) in heavy-metal/FM bilayers [40–43], both of which are efficient and scalable in spintronic devices. In both schemes, an alternating charge current generates an oscillating spin current that exerts a spin torque on the magnetization. Particularly in SOT-based devices, the in-plane current is more easily tuned than the perpendicular current, enabling finer control of the alternating driving torque. In addition, the role of the inertial effects in mode polarization has received limited attention in the literature. Authors of prior studies on spin dynamics driven by SOTs in inertial magnetic materials have implicitly assumed that the handedness and polarization are essentially fixed by the material. A systematic investigation of the polarization of resonant modes and its tuning by driving forces is, to the best of our knowledge, lacking in the literature.

Motivated by the above considerations, we present the investigation of inertial resonant modes in AFMs driven by alternating SOTs. We show that SOTs generated by two orthogonal in-plane currents tune the polarization state (linear, elliptical, or circular) and handedness (left or right handed) of both precessional and nutational AFM resonances. We find that the handedness reverses at critical current ratios that depend explicitly on the inertial relaxation time. These inertia-dependent switching points provide a practical route to determine spin inertia across a broad range of materials. We use chirality and handedness interchangeably, following common usage in the literature.

II. MODEL

As illustrated in Fig. 1, we study an inertial AFM film attached to a heavy metal (HM) with strong spin-orbit coupling, driven by oscillating in-plane currents. The bipartite AFM dynamics are captured phenomenologically by two exchange-coupled ILLG equations, which include spin inertia, Gilbert damping, and SOTs. For sublattice k, the ILLG equation reads

$$\frac{d\mathbf{m}_k}{dt} = \mathbf{m}_k \times \frac{d\mathcal{E}}{d\mathbf{m}_k} + \alpha \mathbf{m}_k \times \frac{d\mathbf{m}_k}{dt} + \eta \mathbf{m}_k \times \frac{d^2\mathbf{m}_k}{dt^2} + \boldsymbol{\tau}_k, \tag{1}$$

where $\mathbf{m}_k$ is the unit magnetization vector of sublattice k ($k = 1, 2$), α is the Gilbert damping constant, and η is the inertial relaxation time, typically ranging from femtoseconds to picoseconds, as predicted by *ab initio* calculations [44] and confirmed experimentally [13–15].

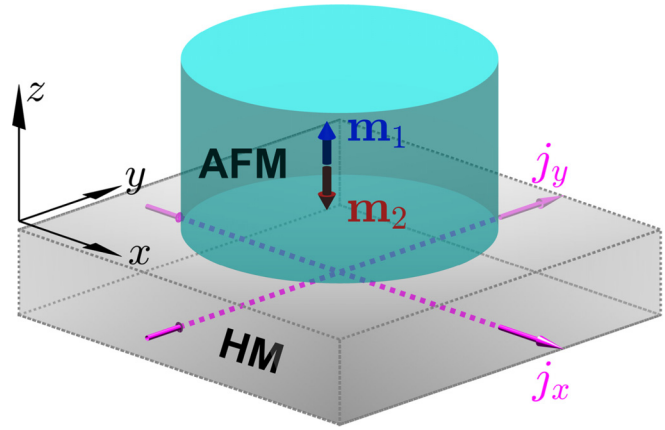


FIG. 1. Schematic diagram of model.

The magnetic energy, arising from the magnetocrystalline anisotropy and the intersublattice exchange interaction, is expressed in frequency units as

$$\mathcal{E} = \omega_E \mathbf{m}_1 \cdot \mathbf{m}_2 + \omega_K \sum_k (\mathbf{m}_k \cdot \mathbf{e}_z)^2, \tag{2}$$

where $\omega_{E(K)} = \gamma_0 H_{E(K)}$, with H_E and H_K being the exchange field and the anisotropy field, respectively. Here, $\gamma_0 = g\mu_0\mu_B/\hbar$ is the gyromagnetic ratio with g being the Landé g factor, μ_0 the vacuum susceptibility, μ_B the Bohr magneton, and $\hbar$ the reduced Planck constant. The anisotropy easy axis is oriented perpendicular to the film plane.

The last term in Eq. (1) represents the SOTs, originating from spin transfer between the local magnetization and spin currents generated in the adjacent HM layer. Including both dampinglike and fieldlike components [45], the SOTs are given by

$$\boldsymbol{\tau}_k = -\rho\{\mathbf{m}_k \times [\mathbf{m}_k \times (\mathbf{e}_z \times \mathbf{j}_e)] + \beta \mathbf{m}_k \times (\mathbf{e}_z \times \mathbf{j}_e)\}, \tag{3}$$

where β is the ratio of fieldlike to dampinglike SOT.

The prefactor $\rho = \xi\mu_B/(eM_s d)$ sets the overall SOT strength. Here, M_s is the saturation magnetization of sublattice, d denotes the thickness of the AFM layer, and e is the elementary charge. The SOT efficiency is defined as $\xi = T_{\text{int}}\theta_{\text{sh}}$ [46,47], where θ_{sh} is the spin Hall angle [45] and T_{int} the spin transparency [48] of the HM/AFM interface. The dampinglike SOT is nonconservative. It represents the antidamping torque that is even under $\mathbf{m}_k \to -\mathbf{m}_k$. It can be written as a torque from an effective field $\mathbf{H}_{\text{DL}} \propto \mathbf{m}_k \times \mathbf{p}$, where $\mathbf{p} \equiv \mathbf{e}_z \times \mathbf{j}_e$, thereby modifying the effective Gilbert damping in linear response. The fieldlike SOT is precessional conservative torque that is odd under $\mathbf{m}_k \to -\mathbf{m}_k$. It induces precession about an effective field $\mathbf{H}_{\text{FL}} \propto \mathbf{p}$, where $\mathbf{p}$ is the spin-polarization direction set by the spin Hall effect in the HM.

The in-plane electric current density $\mathbf{j}_e$ is expressed in components as

$$\mathbf{j}_e = j_x \mathbf{e}_x + j_y \mathbf{e}_y. \tag{4}$$

To excite stationary modes, in-plane alternating electric currents are applied, as shown in Fig. 1. For analytical convenience, the current is expressed in complex form $(j_x, j_y) = (J_x, iJ_y)e^{-i\omega t}$, where $J_{x(y)} > 0$ denote the current amplitudes.

In this representation, the phase of j_y leads (lags) that of j_x by 90° for positive (negative) ω, corresponding to right-handed (left-handed) polarized SOTs. Taking the real part yields the physical current $J_x \cos\omega t\, \mathbf{e}_x + J_y \sin\omega t\, \mathbf{e}_y$.

Each term in the ILLG equation encodes a distinct physical mechanism. The precessional term $\mathbf{m}_k \times d\mathcal{E}/d\mathbf{m}_k$ drives conservative motion in the effective field $\mathbf{H}_{\rm eff} = d\mathcal{E}/d\mathbf{m}_k$ set by the magnetic potential energy. The Gilbert term represents dissipation due to coupling of the magnetic moments to a thermal bath. The spin-inertial term accounts for the dynamics related to the kinetic energy. The spin-orbit terms capture the external torques exerted by the HM layer on the AFM film. Although each contribution is well understood, their competition produces the nontrivial dynamics analyzed in Secs. III–V.

One of the issues in inertial spin dynamics is the applicable timescale, set by the inertial relaxation time. Reported values span orders of magnitude: estimates near 1 fs were proposed in Ref. [2] and inferred from FM-resonance precession data in Ref. [13]. First-principles calculations [44] gave values $\eta \approx$ 1–100 fs. *Ab initio* simulations [49] of the dynamical magnetic susceptibility indicated $\eta \sim$ 10–100 fs. Time-resolved magneto-optical detection of resonant nutation [14] yielded $\eta \sim 100$ fs. Measurements on cobalt films [15] reported $\eta/\alpha \approx 750$ fs. Given the wide range of reported values for the inertial relaxation time, we present results as a function of η.

III. RESONANT SPECTRUM

Due to the uniaxial anisotropy and intersublattice exchange [Eq. (2)], the static equilibrium magnetizations of the two sublattices align along the $\pm z$ directions, respectively. For small deviations from equilibrium, the z components of the magnetizations remain unchanged to first order, such that $m_1^z \approx 1$ and $m_2^z \approx -1$. To describe the magnetic response of the AFM in the linear regime, we adopt the ansatz $\mathbf{m}_k = (-1)^{k+1}\mathbf{e}_z + m_k^x(t)\mathbf{e}_x + m_k^y(t)\mathbf{e}_y$, where $m_k^x(t)$, $m_k^y(t)$ are complex-valued functions encoding the amplitude and phase of the response to SOTs. Inserting the ansatz into Eq. (1), assuming a harmonic time dependence of $m_k^x(t)$, $m_k^y(t)$ (i.e., replacing d/dt by $-i\omega$) and keeping only terms linear in $m_k^x(t)$, $m_k^y(t)$, j_x, and j_y, one obtains a four-dimensional linear inhomogeneous system of ordinary differential equations that describes damped magnetic oscillations driven by periodic forces. As detailed in Appendix A, solving this system yields the steady-state linear response modes

$$\begin{bmatrix} m_1^x(t) \\ m_1^y(t) \\ m_2^x(t) \\ m_2^y(t) \end{bmatrix} = \frac{\rho}{\Delta} \begin{pmatrix} \chi_1 & \chi_2 \\ -\chi_2 & \chi_1 \\ -\chi_1 & \chi_2 \\ -\chi_2 & -\chi_1 \end{pmatrix} \begin{bmatrix} j_x(t) \\ j_y(t) \end{bmatrix}, \tag{5}$$

where $\chi_1 = (\eta\omega^2 - 2\omega_E - \omega_K) + i(\alpha - \beta)\omega$, $\chi_2 = \beta(\eta\omega^2 - \omega_K) + i(1 + \alpha\beta)\omega$, and

$$\Delta = (\Omega_1 - i\alpha\omega)(\Omega_2 - i\alpha\omega) - \omega^2, \tag{6}$$

with

$$\Omega_1 = 2\omega_E + \omega_K - \eta\omega^2, \tag{7}$$

$$\Omega_2 = \omega_K - \eta\omega^2. \tag{8}$$

In Eq. (5), a susceptibility tensor is defined to characterize the linear response to alternating SOTs, in analogy with the Polder susceptibility tensor [50] describing the linear response to an alternating magnetic field.

To analyze the properties of the steady-state modes, it is convenient to take the real part of Eq. (5). The resulting harmonic oscillations of the magnetization driven by alternating SOTs with frequency ω are given by

$$m_k^{x(y)} = \mathcal{A}_k^{x(y)} \cos\left[\omega t + \phi_k^{x(y)}\right]. \tag{9}$$

The polarization degree of the linear modes is set by the ratio $\mathcal{A}_k^y/\mathcal{A}_k^x$, while the phase difference between m_k^x and m_k^y determines the handedness of $\mathbf{m}_k$. In Eq. (9), the amplitudes are

$$\mathcal{A}_{1,2}^{x(y)} = \rho\sqrt{\frac{P_1 J_{x(y)}^2 + P_2 J_{y(x)}^2 \pm P_3 J_x J_y}{\widetilde{\Delta}}}, \tag{10}$$

where upper and lower signs represent sublattices 1 and 2, respectively. This sign convention is maintained throughout unless stated otherwise. To simplify the expressions, we introduce $P_1 = (\alpha - \beta)^2\omega^2 + \Omega_1^2$, $P_2 = (1 + \alpha\beta)^2\omega^2 + \beta^2\Omega_2^2$, $P_3 = 2\omega[2(1 + \alpha\beta)\omega_E + (1 + \beta^2)\Omega_2]$, and

$$\widetilde{\Delta} = [(1 - \alpha^2)\omega^2 - \Omega_1\Omega_2]^2 + 4\alpha^2\omega^2\left(\omega^2 + \omega_E^2\right). \tag{11}$$

The phases in Eq. (9) are written as

$$\phi_{1,2}^x = \tan^{-1}(\pm Q_1 J_x + Q_2 J_y, \pm Q_3 J_x + Q_4 J_y), \tag{12}$$

$$\phi_{1,2}^y = \tan^{-1}(Q_4 J_x \pm Q_3 J_y, -Q_2 J_x \mp Q_1 J_y), \tag{13}$$

where $\tan^{-1}(x, y)$ denotes the two-argument arctangent that returns the angle of the vector (x, y), correctly resolving the quadrant [51]. In Eqs. (12) and (13), the coefficients before $J_{x,y}$, relying on ω, are given by $Q_1 = (1 + \alpha\beta)\Omega_1\omega^2 - [\alpha(\alpha - \beta)\omega^2 + \Omega_1^2]\Omega_2$, $Q_2 = \omega\{(1+\alpha^2)(1+\alpha\beta)\omega^2 + [\alpha\beta\Omega_2 - \Omega_1]\Omega_2\}$, $Q_3 = \omega\{(1 + \alpha^2)(\alpha - \beta)\omega^2 + [\alpha\Omega_1 + \beta\Omega_2]\Omega_1\}$, and $Q_4 = (\alpha - \beta)\Omega_2\omega^2 + [\alpha(1 + \alpha\beta)\omega^2 + \beta\Omega_2^2]\Omega_1$. Equations (12) and (13) show that the phase lag of the stationary forced oscillations relative to the driving SOTs depends on the amplitude ratio J_x/J_y and on the driving frequency ω.

The handedness of the linear modes is determined by the phase difference between the x and y components of $\mathbf{m}_{1,2}$. From Eqs. (12) and (13), one obtains the difference

$$\Delta\phi_{1,2} \equiv \phi_{1,2}^x - \phi_{1,2}^y = \tan^{-1}(X_{1,2}, Y_{1,2}), \tag{14}$$

where $X_{1,2} = \pm(Q_1 Q_4 - Q_2 Q_3)(J_x^2 - J_y^2)$, and $Y_{1,2} = \pm(Q_1 Q_2 + Q_3 Q_4)(J_x^2 + J_y^2) + (Q_1^2 + Q_2^2 + Q_3^2 + Q_4^2)J_x J_y$. Note that, when flipping the sign of ω, Q_1 and Q_4 remain unchanged, and Q_2 and Q_3 change the sign. Consequently, $X_{1,2}$ do not change, and Y_1 (Y_2) becomes Y_2 (Y_1).

The system shows two SOT-driven resonances: a low-frequency precession and a high-frequency nutation created by spin inertia (Fig. 2). Inertia enters via the $-\eta\omega^2$ terms in $\Omega_{1,2}$, shifting the spectrum and producing the nutation peak. One can see that the precessional resonances are stronger (higher peaks) and occur at lower frequencies than nutational ones. However, both resonances lie in the terahertz range, due to the exchange enhancement characteristic of AFMs. Figure 2 shows the precessional and nutational spectra for

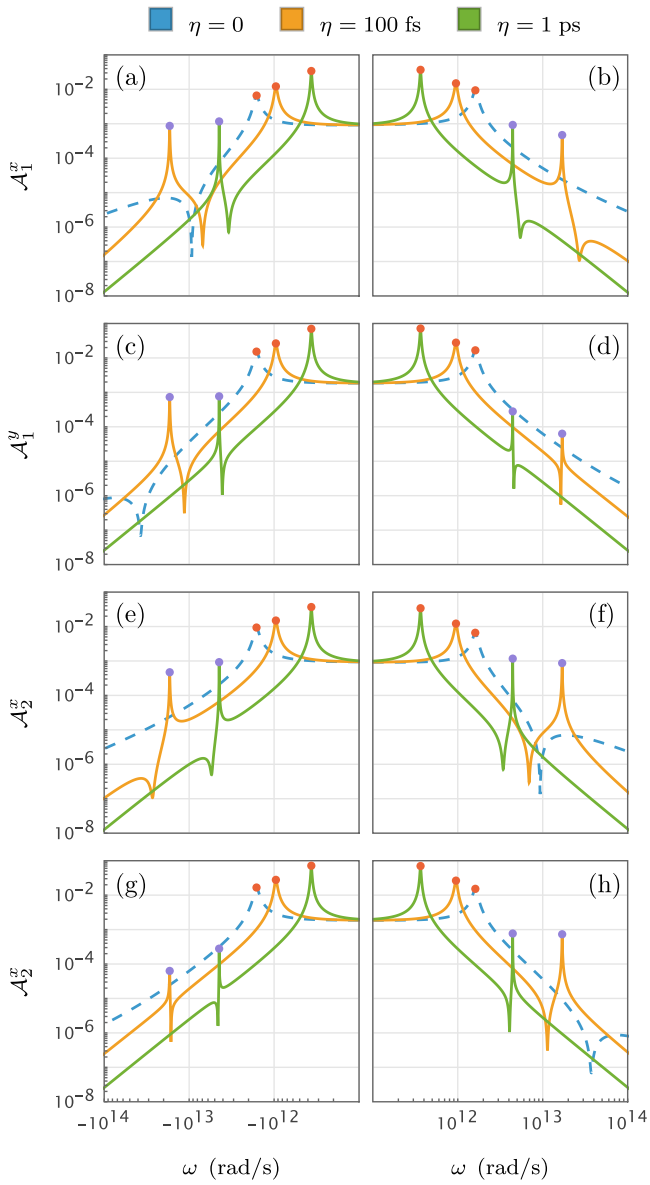


FIG. 2. AFM spectra without spin inertia exhibit the single precessional resonance (dashed lines, $\eta = 0$). Finite spin inertia $\eta > 0$ shifts the precessional AFM resonance and induces the additional nutational resonances (solid lines). Peaks labeled with red (purple) points correspond to precessional (nutational) resonances. Both axes are shown on a logarithmic scale; low-frequency parts are omitted for clarity. Curves are evaluated from Eq. (10) using $\omega_E = 9.25$ THz, $\omega_K = 0.14$ THz, $\alpha = 0.01$, $\beta = 0.02$, $J_x = 1\,\mathrm{GA/m^2}$, $J_y = 2\,\mathrm{GA/m^2}$, and $\rho \approx 0.13\,\mathrm{Hz/(A/m^2)}$. The values of ω_E, ω_K, and ρ are derived from the magnetic parameters of MnF_2 [52] for a film thickness $d = 3$ nm and SOT efficiency $\xi = 0.32$.

different inertial relaxation times η, considering the general case $J_x \neq J_y$. The left (right) column displays spectra at negative (positive) frequencies. It is important to note that panels (a) and (b), (c) and (d), (e) and (f), and (g) and (h) reveal an asymmetry of the spectra with respect to frequency inversion for a given sublattice. Additionally, comparing panels (a) and (f), (b) and (e), (c) and (h), and (d) and (g), one observes that the positive-frequency spectrum of $m_1^{x,y}$ mirrors the negative-frequency spectrum of $m_2^{x,y}$ and vice versa. This can be understood from symmetry arguments: Exchanging the sublattices ($\mathcal{A}_1^{x,y} \leftrightarrow \mathcal{A}_2^{x,y}$) is equivalent to time reversal ($\omega \leftrightarrow -\omega$). Therefore, the spectra are symmetric under the combined transformation $1 \leftrightarrow 2$ and $\omega \leftrightarrow -\omega$.

IV. RESONANT PEAK AND FREQUENCY

From Eqs. (10) and (11) and noting that $\alpha^2 \ll 1$, the amplitudes of the linear modes increase at resonance, which occurs when

$$\omega^2 = \Omega_1 \Omega_2, \tag{15}$$

where $\Omega_{1,2}$ are defined in Eqs. (7) and (8). Solving Eq. (15) yields the resonant frequencies, which appear in pairs $\pm\omega$. In the absence of spin inertia ($\eta = 0$), the resonance condition gives $\omega = \pm\sqrt{\omega_K(2\omega_E + \omega_K)}$. In the presence of inertia, the nutational frequency ω_n and the precessional frequency ω_p are given by

$$\omega_{n,p} = \sqrt{\left(\frac{\kappa_{n,p}}{2\eta}\right)^2 - \omega_E^2}, \tag{16}$$

where

$$\kappa_{n,p} = \sqrt{(1 + 2\eta\omega_E)^2 + 4\eta\omega_K} \pm 1, \tag{17}$$

with the upper (lower) sign corresponding to nutation (precession). The resonant frequencies exhibit strong dependence on the inertial relaxation time η, as shown in Fig. 3(a).

Since the exchange interaction dominates the dynamics in AFMs, the precessional resonance is enhanced into the terahertz regime. At the same time, the nutational frequency is significantly higher than in FMs. Moreover, spin inertia induces a pronounced redshift in the resonant frequencies of both nutation and precession, as also evident in the spectra shown in Fig. 2.

In general, resonant peak heights quantify the energy stored in the forced oscillations. As illustrated in Fig. 2, these heights depend on the inertial relaxation time η and differ for positive and negative frequencies. Therefore, it is necessary to analyze them in detail. Substituting the resonant frequencies in Eq. (16) into Eqs. (10) and (11) yields explicit expressions for the peak heights, which are different for each sublattice and each component of magnetization. For the ω_n-branch resonance, the peak heights of $x(y)$ components of sublattices 1 and 2 are as follows:

$$\mathcal{N}_{1,2}^{x(y)} = \rho\frac{\eta}{\sqrt{2}\alpha\kappa_n}\sqrt{\frac{\kappa_n - 2\eta\omega_E}{2\eta(\omega_E + \omega_K) + \kappa_n}} \times |\sqrt{\kappa_n - 2\eta\omega_E}J_{x(y)} \mp \sqrt{\kappa_n + 2\eta\omega_E}J_{y(x)}|. \tag{18}$$

For the ω_p-branch resonance, the heights of $x(y)$ components of sublattices 1 and 2 are given by

$$\mathcal{P}_{1,2}^{x(y)} = \rho\frac{\eta}{\sqrt{2}\alpha\kappa_p}\sqrt{\frac{\kappa_p + 2\eta\omega_E}{2\eta(\omega_E + \omega_K) - \kappa_p}} \times |\sqrt{\kappa_p - 2\eta\omega_E}J_{x(y)} \pm \sqrt{\kappa_p + 2\eta\omega_E}J_{y(x)}|. \tag{19}$$

The peak heights of the negative ($-\omega_n$ and $-\omega_p$) branches are obtained by interchanging sublattices 1 and 2 in Eqs. (18)

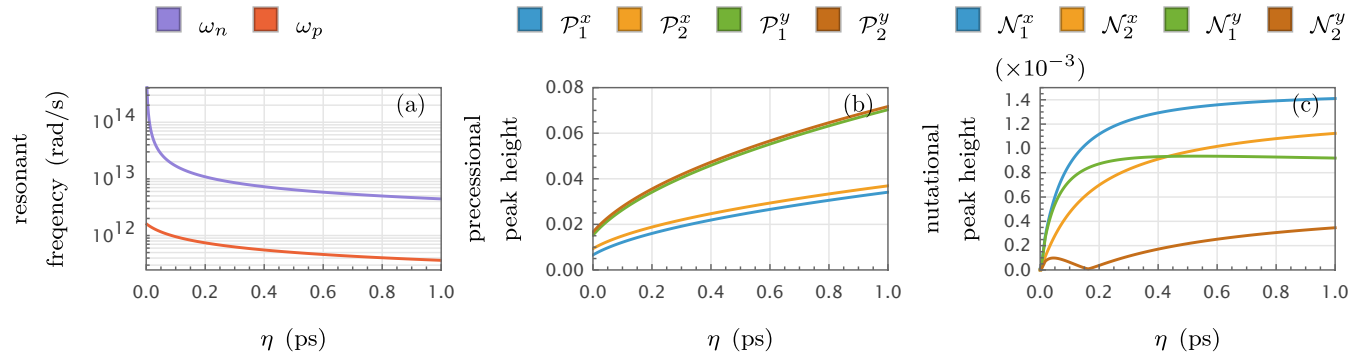


FIG. 3. (a) Resonant frequencies as a function of η. Curves are computed from Eq. (16). A logarithmic scale is used on the frequency axis, and low-frequency regions are omitted for clarity. (b) and (c) show the dependence of peak heights on η for precession and nutation, respectively. Curves are computed from Eqs. (19) and (18). The parameters used are the same as in Fig. 2.

and (19), respectively. Throughout the derivation, we assume $\alpha^2 \ll 1$, $\alpha\beta \ll 1$, and $\beta^2 \ll 1$.

Equations (18) and (19) reveal several notable features. (i) The peak heights are highly sensitive to the relative magnitudes of J_x and J_y. For the generic case $J_x \neq J_y$, as shown in Figs. 3(b) and 3(c), the x and y components exhibit unequal peak heights, indicating elliptical polarization of the resonant modes. Spin inertia further enhances the ellipticity. (ii) Only when $J_x = J_y$ do the x and y components exhibit equal peak heights, corresponding to circularly polarized modes. In this case, all four resonances at $\pm\omega_n$ and $\pm\omega_p$ exist. This contrasts with the FM case, where only two modes ($-\omega_n$ and ω_p) appear, as seen in Figs. 7(e) and 7(f). (iii) The nutational peaks are generally much smaller than the precessional ones, as evident from comparison between Figs. 3(b) and 3(c). In the limit $\eta = 0$, one has $\kappa_n = 2$, and thus, $\mathcal{N}_{1,2}^x = \mathcal{N}_{1,2}^y = 0$, indicating the absence of nutation. Meanwhile, $\kappa_p = 0$ for $\eta = 0$. Then taking the limit $\eta \to 0$ in Eq. (19), the precessional peak heights approach

$$\frac{\rho}{2\alpha}\frac{|\sqrt{2\omega_E+\omega_K}J_{x(y)} \pm \sqrt{\omega_K}J_{y(x)}|}{(\omega_E+\omega_K)\sqrt{\omega_K}}, \tag{20}$$

which corresponds to the resonant peak heights of AFM sublattices in the absence of spin inertia. (iv) For specific ratios of J_x and J_y, certain nutational peak vanishes. For example, when $J_y/J_x = \sqrt{(\kappa_n + 2\eta\omega_E)/(\kappa_n - 2\eta\omega_E)}$, one finds $\mathcal{N}_1^y = 0$, as indicated by the brown curve in Fig. 3(c). Complete suppression of this nutational peak enables polarization tuning from circular to linear.

V. ANALYSES OF POLARIZATION AND HANDEDNESS

To characterize the resonance polarization, we employ two quantities: the ellipticity, which measures the degree of polarization, and the handedness, extracted from the phase difference between m_x and m_y. The ellipticity is defined as the aspect ratio m_y/m_x: It equals 1 for circular polarization and tends to 0 or ∞ for linear polarization; intermediate values correspond to elliptical polarization. For the nutational modes, we introduce ellipticity as $e_{1,2}^n = \mathcal{N}_{1,2}^y/\mathcal{N}_{1,2}^x$, and for the precessional modes, $e_{1,2}^p = \mathcal{P}_{1,2}^y/\mathcal{P}_{1,2}^x$, where the subscripts 1,2 label the two sublattices. Using Eqs. (18) and (19), we obtain

$$e_{1,2}^n = \left|\frac{r_n J_x \mp J_y}{J_x \mp r_n J_y}\right|, \tag{21}$$

$$e_{1,2}^p = \left|\frac{r_p J_x \pm J_y}{J_x \pm r_p J_y}\right|, \tag{22}$$

where

$$r_{n,p}(\eta) = \sqrt{\frac{\sqrt{(1+2\eta\omega_E)^2+4\eta\omega_K} \pm 1 + 2\eta\omega_E}{\sqrt{(1+2\eta\omega_E)^2+4\eta\omega_K} \pm 1 - 2\eta\omega_E}}. \tag{23}$$

In the limit $\eta \to 0$, one recovers $r_p = \sqrt{(2\omega_E+\omega_K)/\omega_K}$ and $r_n = 1$. Equations (21) and (22) are written for the positive-frequency branches; the corresponding expressions for negative frequencies follow by exchanging the sublattice indices $1 \leftrightarrow 2$.

The degree of polarization, characterized by the ellipticity, strongly depends on the ratio J_y/J_x and the inertial relaxation time η, as shown in the upper panels of Fig. 4. Given similar behaviors for opposite signs of $J_{x,y}$ and resonant frequency, the analysis is restricted to $J_{x,y} > 0$ and positive frequencies.

For the nutational mode, $\mathbf{m}_1$ becomes linearly polarized along the x axis (y axis) when $J_y/J_x = r_n$ ($J_y/J_x = 1/r_n$), as indicated by the vanishing (diverging) ellipticity e_1^n in Fig. 4(a) with red arrows. In contrast, Fig. 4(c) shows that e_2^n remains finite and nonunity at these points, indicating elliptical polarization for $\mathbf{m}_2$. Thus, the nutational mode can be linearly polarized in one sublattice and elliptically polarized in the other.

A similar feature appears in the precessional mode: At $J_y/J_x = r_p$ ($J_y/J_x = 1/r_p$), $\mathbf{m}_2$ becomes linearly polarized along the x axis (y axis), while $\mathbf{m}_1$ remains elliptically polarized, as seen in Figs. 4(e) and 4(g). The linear polarization is indicated with red arrows.

In the limiting case where J_x or J_y vanishes, all modes are elliptically polarized with ellipticity equal to $r_{n,p}$ or $1/r_{n,p}$. When $J_x = J_y$, the ellipticity becomes unity, and all modes are circularly polarized. These polarization characteristics are also illustrated schematically in Fig. 5 for representative values of J_y/J_x, in agreement with Fig. 4. Comparison of the ellipticity curves for different η values reveals that

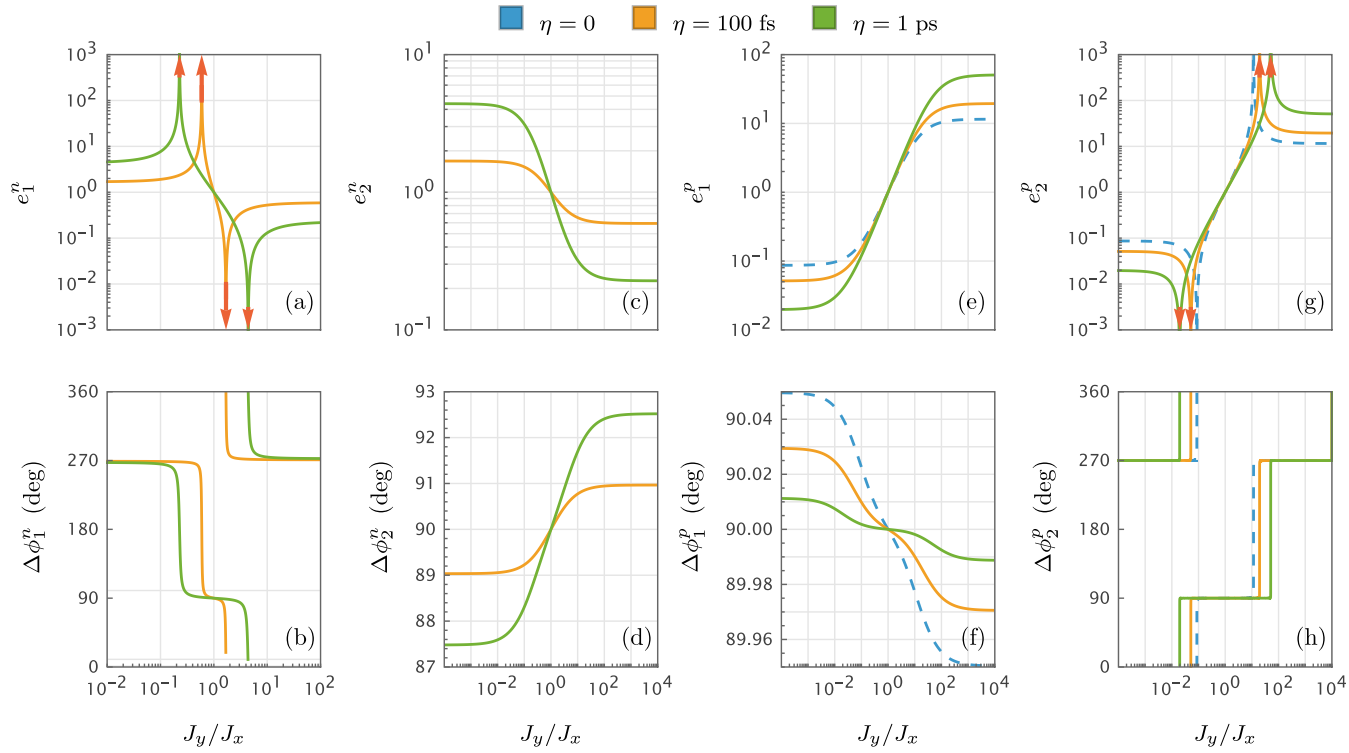


FIG. 4. Ellipticity (upper row) and intercomponent phase difference (lower row) as functions of the current ratio J_y/J_x at positive frequencies for several values of η. Panels (a)–(d) present the nutational modes of sublattices 1 and 2, while (e)–(h) display the corresponding precessional modes. The curves are calculated with Eqs. (21), (22), and (24). Parameters are identical to those in Fig. 2.

increasing spin inertia enhances the deviation of $e_{1,2}^n$ and $e_{1,2}^p$ from unity, thereby increasing the ellipticity and, thus, the degree of polarization.

In addition to ellipticity, the handedness—the sense of rotation of $\mathbf{m}_{1,2}$ around the z axis—completes the description of the polarization. Let $\mathbf{m}_\perp = m_k^x \mathbf{e}_x + m_k^y \mathbf{e}_y$ denote the in-plane magnetization. As outlined in Figs. 6(a) and 6(b), a mode is righthanded if $\mathbf{e}_z \cdot (\mathbf{m}_\perp \times d\mathbf{m}_\perp/dt) > 0$ or, equivalently, if $\omega \sin(\phi_k^x - \phi_k^y) > 0$ according to Eq. (9). The sign inversion corresponds to the opposite handedness.

At resonance, the phase differences defined in Eq. (14) can be simplified as

$$\Delta\phi_{1,2}^{n(p)} = \tan^{-1}\left[X_{1,2}^{n(p)}, Y_{1,2}^{n(p)}\right], \tag{24}$$

where for the $\omega_n(\omega_p)$-branch resonance,

$$X_{1,2}^{n(p)} = \pm\alpha\omega_{n(p)}^2\left(J_y^2 - J_x^2\right), \tag{25}$$

$$Y_{1,2}^{n} = \mp\frac{\kappa_n - 2\eta\omega_E}{4\eta^2}\left(\sqrt{\kappa_n - 2\eta\omega_E}J_x \mp \sqrt{\kappa_n + 2\eta\omega_E}J_y\right) \times \left(\sqrt{\kappa_n + 2\eta\omega_E}J_x \mp \sqrt{\kappa_n - 2\eta\omega_E}J_y\right), \tag{26}$$

$$Y_{1,2}^{p} = \pm\frac{\kappa_p + 2\eta\omega_E}{4\eta^2}\left(\sqrt{\kappa_p - 2\eta\omega_E}J_x \pm \sqrt{\kappa_p + 2\eta\omega_E}J_y\right) \times \left(\sqrt{\kappa_p + 2\eta\omega_E}J_x \pm \sqrt{\kappa_p - 2\eta\omega_E}J_y\right), \tag{27}$$

where $\kappa_{n,p}$ has been defined in Eq. (17). The phase differences for the $-\omega_{n,p}$ branches follow by exchanging the sublattice indices $1 \leftrightarrow 2$ in Eqs. (25)–(27). In deriving Eq. (24), we insert the resonant frequencies for ω and use the approximations $\alpha^2 \ll 1$, $\alpha\beta \ll 1$, and $\beta^2 \ll 1$. For positive resonant frequencies (righthanded SOTs), the mode is righthanded when $0^\circ < \Delta\phi_{1,2}^{n(p)} < 180^\circ$ and lefthanded when $180^\circ < \Delta\phi_{1,2}^{n(p)} < 360^\circ$.

Analogous to the ellipticity, the phase difference $\Delta\phi_{1,2}^{n(p)}$ between the x and y components is governed by the ratio J_y/J_x (lower panels of Fig. 4). For the nutational branch, the phase difference is $\Delta\phi_1^n = 0^\circ$ at $J_y/J_x = r_n$ and $\Delta\phi_1^n = 180^\circ$ at $J_y/J_x = 1/r_n$ [Fig. 4(b)]. Hence, m_1^x and m_1^y oscillate in phase at $J_y/J_x = r_n$ or antiphase at $J_y/J_x = 1/r_n$, whereas $\mathbf{m}_1$ is linearly polarized. In the precessional branch, $\Delta\phi_2^p = 180^\circ$ ($\Delta\phi_2^p = 0^\circ$) at $J_y/J_x = r_p$ ($J_y/J_x = 1/r_p$) [Fig. 4(h)], again indicating that $\mathbf{m}_2$ is linear polarized. The nutational mode $\mathbf{m}_2$ and precessional mode $\mathbf{m}_1$ exhibit the opposite trends with increasing the inertial relaxation time η, i.e., the phase difference $\Delta\phi_2^n$ increases with η, whereas $\Delta\phi_1^p$ decreases.

In the limiting case $J_x \to 0$ or $J_y \to 0$ and using $\omega_K \ll \omega_E$, in Eqs. (25)–(27), one finds $\Delta\phi \to 270^\circ$ for the nutational mode of $\mathbf{m}_1$ and the precessional mode of $\mathbf{m}_2$, indicating lefthanded polarization. In contrast, $\Delta\phi$ approaches 90° for the nutational mode of $\mathbf{m}_2$ and the precessional mode of $\mathbf{m}_1$, corresponding to righthanded polarization. When $J_x = J_y$, all modes exhibit $\Delta\phi = 90^\circ$, indicating right-handed circular polarization.

Using Eqs. (24)–(27), the polarization handedness of the nutational and precessional resonant modes in sublattices 1 and 2 can be determined by the sign of $\omega_r \sin\Delta\phi_{1,2}^{n(p)}$, where ω_r denotes the resonant frequency. According to this criterion, the condition $\sin\Delta\phi_{1,2}^{n(p)} = 0$ defines the boundaries between

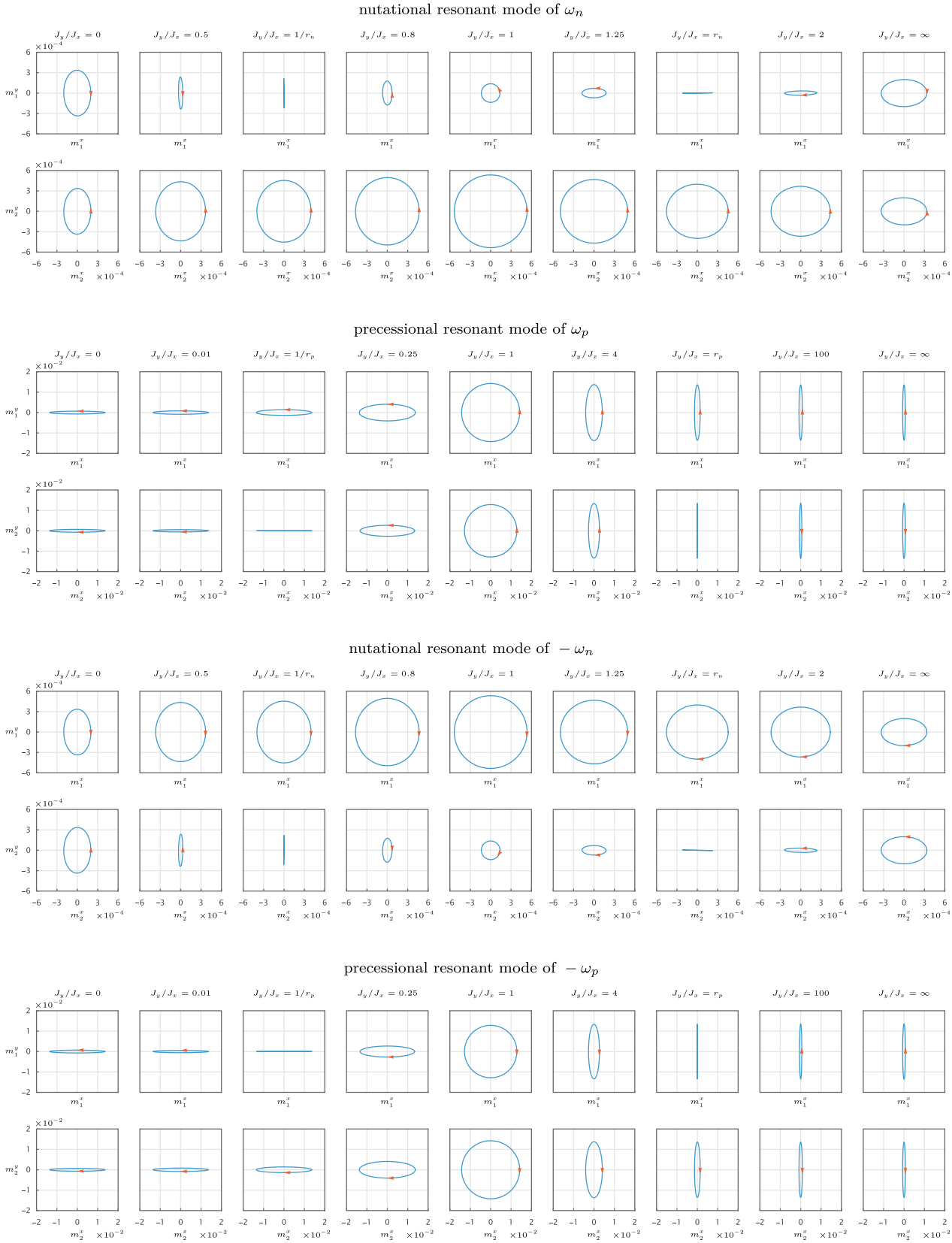
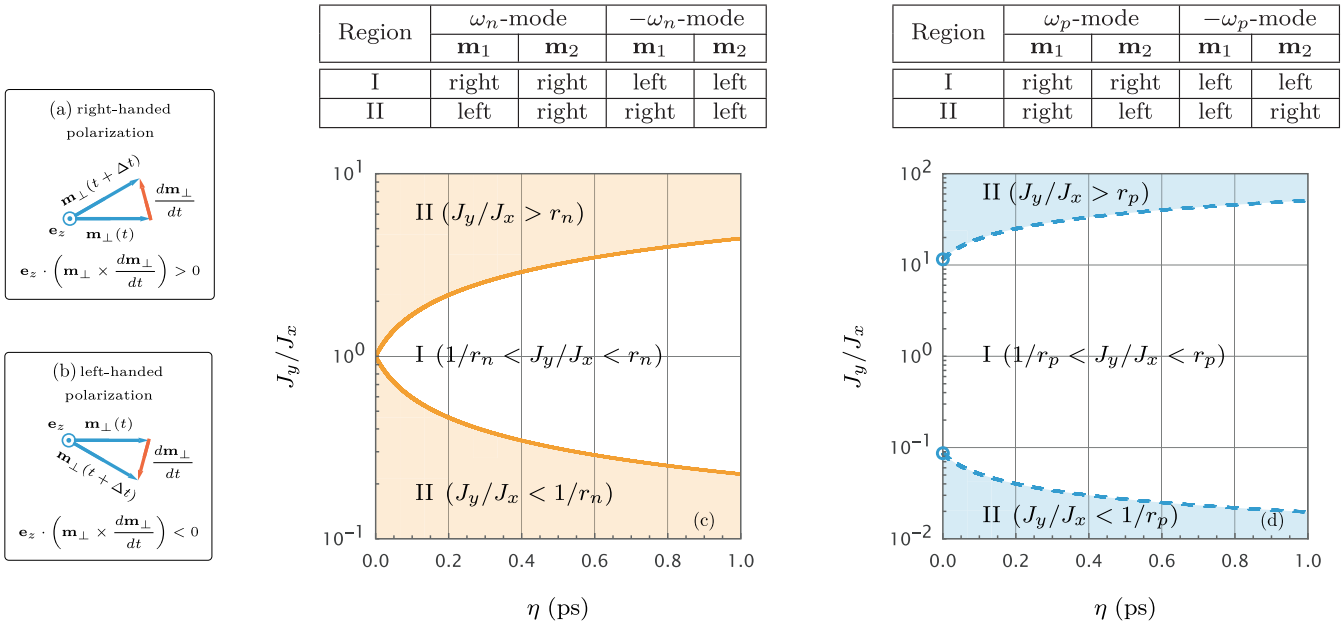


FIG. 5. Polarization and handedness of resonant modes for four branches ($\pm\omega_p$, $\pm\omega_n$) at various values of J_y/J_x. The inertial relaxation time is set to $\eta = 100$ fs, yielding $r_n = 1.6855$ and $r_p = 19.4488$ from Eq. (23). In each panel, the horizontal and vertical axes correspond to m_x and m_y components, respectively. Curves represent the magnetization orbits, and arrows indicate the sense of rotation. In the panels in columns 1–5, $J_x = 1\,\mathrm{GA/m^2}$, and J_y is calculated by the ratio J_y/J_x. In the panels in columns 6–9, $J_y = 1\,\mathrm{GA/m^2}$, and J_x is calculated by the ratio.



Region	ω_n-mode		$-\omega_n$-mode	
	$\mathbf{m}_1$	$\mathbf{m}_2$	$\mathbf{m}_1$	$\mathbf{m}_2$
I	right	right	left	left
II	left	right	right	left

Region	ω_p-mode		$-\omega_p$-mode	
	$\mathbf{m}_1$	$\mathbf{m}_2$	$\mathbf{m}_1$	$\mathbf{m}_2$
I	right	right	left	left
II	right	left	left	right

FIG. 6. (a) and (b) Definition of handedness. Phase diagrams illustrating the polarization of $\mathbf{m}_{1,2}$ as functions of J_y/J_x and η for (c) nutational and (d) precessional resonances. In (c), the upper (lower) boundary is given by $J_y/J_x = r_n$ ($J_y/J_x = 1/r_n$); in (d), by $J_y/J_x = r_p$ ($J_y/J_x = 1/r_p$). The upper and lower circles in (d) mark $J_y/J_x = \sqrt{(2\omega_E + \omega_K)/\omega_K}$ and $\sqrt{\omega_K/(2\omega_E + \omega_K)}$, respectively. The tables above (c) and (d) contain the handedness in different regions for nutational and precessional resonant modes, respectively.

regions of different handedness. These boundaries correspond precisely to $J_y/J_x = r_{n,p}$ and $J_y/J_x = 1/r_{n,p}$, where $r_{n,p}$ is given in Eq. (23).

Based on this analysis, we construct the phase diagrams shown in Figs. 6(c) and 6(d), mapping the polarization types in the parameter space spanned by η and J_y/J_x. The boundary curves in Fig. 6 are calculated using the approximate analytical expression in Eq. (23). The shaded and unshaded regions are determined by evaluating the sign of $\omega_r \sin \Delta\phi_{1,2}$, where $\Delta\phi_{1,2}$ is computed from Eq. (14) using the corresponding resonant frequencies. The analytical approximations agree very well with the exact numerical results.

From the above analysis—particularly Figs. 5 and 6—it is evident that the polarization of resonant modes can be tuned by controlling both the handedness (i.e., the sign of the frequency) and the ellipticity (J_y/J_x) of the alternating driving force (here, SOTs generated by alternating currents). For the sake of clarity, we restrict the discussion to positive $J_{x,y}$, such that the handedness of the driving force is solely determined by the sign of its frequency.

For both nutational and precessional modes, the polarization of all resonant modes matches that of the SOTs when the ellipticity of the drive is close to 1, that is, when $1/r_n < J_y/J_x < r_n$ (nutation) or $1/r_p < J_y/J_x < r_p$ (precession). This corresponds to Region I in Figs. 6(c) and 6(d). In this regime, both $\mathbf{m}_1$ and $\mathbf{m}_2$ rotate righthandedly about the $+z$ axis for positive resonant frequencies, and lefthandedly for negative frequencies, consistent with the behavior shown schematically in Fig. 5.

When the ellipticity of the SOTs deviates more strongly from 1, the polarization behavior becomes sublattice dependent [Region II in Figs. 6(c) and 6(d)]. Specifically, for nutational modes in Region II ($J_y/J_x < 1/r_n$ or $J_y/J_x > r_n$), $\mathbf{m}_1$ rotates lefthandedly, while $\mathbf{m}_2$ maintains righthanded rotation at positive frequency. For precessional modes in Region II ($J_y/J_x < 1/r_p$ or $J_y/J_x > r_p$), the handedness is reversed: $\mathbf{m}_1$ rotates righthandedly, while $\mathbf{m}_2$ rotates lefthandedly for positive frequency. We emphasize that the boundaries of the polarization regions depend sensitively on the inertial relaxation time η, enabling its experimental determination. By tuning the ratio of two orthogonally applied currents and measuring the resulting mode polarizations, η can be extracted by fitting the data with Eqs. (21)–(23).

From Figs. 6(c) and 6(d), we infer that Region I of the nutational mode is much smaller than that of the precessional mode because $r_n \ll r_p$. This is consistent with Eq. (23), which for $\omega_K/\omega_E \ll 1$ gives

$$r_n = \sqrt{1 + 2\eta\omega_E} + O[\omega_K],$$
$$r_p = \sqrt{\frac{2\omega_E}{\omega_K}}\sqrt{1 + 2\eta\omega_E} + O\left[\omega_K^{1/2}\right]. \tag{28}$$

For typical AFM parameters with $\omega_K \ll \omega_E$, it follows that $r_n \ll r_p$. Consequently, the handedness of the nutational mode reverses at a much smaller current difference than that of the precessional mode.

In FMs, as shown in Appendix C and Fig. 8, the handedness of resonant modes is independent of the ratio J_y/J_x. For positive (negative) frequency, the nutational mode is lefthanded (righthanded), while the precessional mode is righthanded (lefthanded). In contrast, the situation in AFMs is more intricate. As J_y/J_x crosses the critical values $r_{n(p)}$ or $1/r_{n(p)}$, the handedness of the nutational (precessional) mode is reversed for one of the sublattices. These critical points depend on the inertial relaxation time η and are a unique feature of AFMs, absent in the FM case.

Finally, the fieldlike SOT [the β term in Eq. (3)] has a negligible impact on the resonance modes. In the peak-height and phase-difference expressions, β enters only through the factors $1+\alpha\beta$ and $1+\beta^2$, and the contribution of the β term is small due to $\alpha\beta \ll 1$ and $\beta^2 \ll 1$ for typical torques induced by the spin Hall effect [45]. Numerical simulations confirm the accuracy of the analytical approximation.

VI. DISCUSSIONS

First, it is worthwhile to elucidate the significance of the negative frequency. When solving the secular equation for a linear oscillating system, the eigenfrequencies usually come in a pair of opposite numbers. For natural oscillation of magnetization, there is no difference between the positive and negative frequency branches, apart from the opposite handedness of oscillating mode. Thus, the negative eigenfrequency has often been thought to be unnecessary. However, the case is somewhat complicated for resonance of magnetization. As shown in Figs. 2 and 7, the peak heights are different at positive and negative resonant frequencies. Also, Fig. 5 indicates that the polarization and handedness of resonant modes are different for positive and negative resonant frequencies. The reason is that the frequency of forced oscillation belongs to the driving force. Different signs of frequency correspond to different handednesses of driving force. As illustrated in above sections, the properties of resonant mode depend on the handedness of driving force, resulting in the asymmetry between positive and negative resonant frequencies.

Second, AFMs host both lefthanded and righthanded spin waves [53], enabling storing information on the handedness (charity) of polarization. This feature has been proposed to design transistors [30,31] and logic gates [32,33] based on spin waves. Thus, it is crucial to detect and manipulate the handedness of spin waves, which has been achieved by inverse spin Hall effect in synthetic AFMs [54]. With regard to the spin waves with zero wave vector, it has been shown that the polarization of resonant mode can be identified and manipulated by using different types of microwave magnetic fields [55]. Here, by steering the degree of polarization (J_y/J_x) and the handedness of the alternating SOTs, we realize the switching of polarization and the reversal of handedness for the nutational and precessional resonant AFM modes. The critical value of J_y/J_x can be tuned by the inertial relaxation time η, as indicated by Eq. (23) and Fig. 6. On the other hand, by varying J_y/J_x and observing the abrupt change of the polarization, one can measure the critical values $J_y/J_x = r_{n,p}$ and then estimate η which, so far, is not experimentally determined for AFMs.

Third, it should be pointed out that we only explore the linear dynamics of AFMs driven by alternating SOTs. The results are suitable for weak driving forces. With the drives becoming stronger, some high-order harmonic magnetic responses gradually emerge. Thus, beyond the linear response described in Eq. (5), $m_k^{x,y}$ should be expanded into a series of harmonics, including the higher-order terms of $j_{x,y}$. Inserting this ansatz and its time derivative into the ILLG equations and collecting terms at each harmonic ($e^{-ni\omega t}, n = 1, 2, 3, \dots$), one arrives at the scalar equations about higher-order susceptibilities by matching the coefficients for every harmonic orders. In general, it is complicated to get explicit analytic solutions for the susceptibilities, and some numeric treatments must be resorted to. Moreover, we use a minimal model of AFMs, in which a perpendicular uniaxial anisotropy is considered. For more complex geometries—for example, involving the biaxial anisotropy, the Dzyaloshinskii-Moriya interaction, and triangular spin textures—the linearization technique can also be used. For noncollinear ground states (e.g., canted AFMs [56]), fluctuations must first be defined in local frames attached to each sublattice, and the equations of motion are then linearized about those frames. Also, by use of the eigenvalues and eigenvectors of linearized system, one can explore the dispersion and polarization of inertial resonant modes. A more thorough understanding of the higher harmonics and further exploration on the complex AFMs are beyond the scope of this work and will be pursued in the future.

Finally, it is interesting to compare the roles of SOTs and spin-transfer torques in driving magnetic resonances. In SOT-based devices, two mutually perpendicular in-plane charge currents can be applied and tuned independently, generating two independent ac driving torques, analogous to two orthogonal in-plane ac magnetic fields. By adjusting the magnitudes and directions (and, if applicable, phases) of these currents, the total driving torque can be engineered to realize different polarizations and handedness. In contrast, in spin-transfer-torque structures, the perpendicular current provides essentially a single driving torque with a fixed direction, which does not allow independent control of the polarization and handedness of the excitation.

VII. CONCLUSIONS

In this paper, we investigate resonant magnetization precession and nutation in a bilayer system composed of a uniaxial AFM and an adjacent HM layer, driven by two in-plane, mutually perpendicular alternating currents. We find that, contrary to the common view that the handedness of a resonant mode is essentially fixed by the material, the polarization state and handedness of both precessional and nutational AFM modes can be controlled by the alternating SOTs generated by in-plane J_x and J_y currents. As the amplitude ratio J_y/J_x of orthogonal driving currents is varied, AFM resonant modes evolve continuously from elliptical to circular and, at critical ratios $r_{n,p}$, to linear polarization. We derive the critical ratios $r_{n,p}$ for the nutational (n) and precessional (p) modes at which a mode becomes linearly polarized and the mode handedness reverse. Moreover, a given mode can be linear on one AFM sublattice while remaining elliptical on the other.

We find that the critical ratios depend explicitly on the inertial relaxation time η and differ between the nutational and precessional resonances, enabling inertia-controlled chirality switching. The polarization and handedness reversals at $r_{n,p}$ provide a practical method to determine inertial relaxation time in SOT-driven AFM resonance experiments.

This tunability is not available in the FM case, where the resonant modes remain nearly circular. A detailed comparison with the FM ILLG case shows that, in FMs, the nutational mode is always lefthanded and the precessional mode always righthanded, and both remain nearly circular regardless of the drive ellipticity. In AFMs, by contrast, both ellipticity and

handedness of the modes depend sensitively on J_y/J_x, η, and the sign of ω. Both nutational and precessional modes appear in pairs at $\pm\omega_{n,p}$, unlike the FM case where certain branches are strongly suppressed for circular driving.

Our findings highlight the richer landscape of polarization and handedness in AFM resonant dynamics and suggest potential applications for AFM modes as carriers of information in spintronic devices. This work advances the fundamental understanding of inertial resonant modes and provides a basis for chirality control in spin-wave-based information processing. We expect that the control of the nutational-mode handedness permits a robust manipulation of nutation magnons in AFMs.

ACKNOWLEDGMENTS

P.-B.H. was supported by the National Science Foundation (NSF) of Changsha City (Grant No. kq2208008) and the NSF of Hunan Province (Grant No. 2023JJ30116). R.-X.W. was supported by the key Program of Education Bureau of Hunan Province (Grant No. 24A0494) and the Regional Joint Funds of the NSF of Hunan Province (Grant No. 2024JJ7312).

DATA AVAILABILITY

The data that support the findings of this article are not publicly available upon publication because it is not technically feasible and/or the cost of preparing, depositing, and hosting the data would be prohibitive within the terms of this research project. The data are available from the authors upon reasonable request.

APPENDIX A: LINEARIZATION OF AFM SYSTEM

To linearize the coupled two-lattices AFM system, it is convenient to expand Eq. (1) in the component form

$$\begin{aligned}\frac{dm_k^x}{dt} &= \omega_E\left(m_k^y m_{3-k}^z - m_k^z m_{3-k}^y\right) - \omega_K m_k^y m_k^z + \alpha\left(m_k^y\frac{dm_k^z}{dt} - m_k^z\frac{dm_k^y}{dt}\right) + \eta\left(m_k^y\frac{d^2m_k^z}{dt^2} - m_k^z\frac{d^2m_k^y}{dt^2}\right)\\ &\quad - \rho\left[j_x m_k^x m_k^y + j_y\left(m_k^{y2} + m_k^{z2}\right)\right] + \rho\beta j_x m_k^z, \qquad \text{(A1)}\\ \frac{dm_k^y}{dt} &= \omega_E\left(m_k^z m_{3-k}^x - m_k^x m_{3-k}^z\right) - \omega_K m_k^z m_k^x + \alpha\left(m_k^z\frac{dm_k^x}{dt} - m_k^x\frac{dm_k^z}{dt}\right) + \eta\left(m_k^z\frac{d^2m_k^x}{dt^2} - m_k^x\frac{d^2m_k^z}{dt^2}\right)\\ &\quad + \rho\left[j_y m_k^x m_k^y + j_x\left(m_k^{z2} + m_k^{x2}\right)\right] + \rho\beta j_y m_k^z, \qquad \text{(A2)}\\ \frac{dm_k^z}{dt} &= \omega_E\left(m_k^x m_{3-k}^y - m_k^y m_{3-k}^x\right) + \alpha\left(m_k^x\frac{dm_k^y}{dt} - m_k^y\frac{dm_k^x}{dt}\right) + \eta\left(m_k^z\frac{d^2m_k^y}{dt^2} - m_k^y\frac{d^2m_k^x}{dt^2}\right)\\ &\quad - \rho\left(j_x m_k^y m_k^z - j_y m_k^z m_k^x\right) - \rho\beta\left(j_x m_k^x + j_y m_k^y\right), \qquad \text{(A3)}\end{aligned}$$

where $k = 1, 2$, denoting the two sublattices. In the main text, it has been assumed that the static equilibrium magnetization lies along the z direction. Thus, for small deviations (m_k^x and m_k^y) from equilibrium, m_k^z is unchanged to first-order in small quantities ($m_1^z \approx 1$ and $m_2^z \approx -1$). For resonance, the excitation sources $j_{x,y}$ are also small quantities. Then keeping only terms linear in m_k^x, m_k^y, j_x, and j_y in Eqs. (A1)–(A3), one can obtain the linear differential equations about m_1^x, m_1^y, m_2^x, and m_2^y, expressed in the matrix form as

$$\begin{pmatrix} 1 & \alpha & 0 & 0\\ -\alpha & 1 & 0 & 0\\ 0 & 0 & 1 & -\alpha\\ 0 & 0 & \alpha & 1\end{pmatrix}\frac{d}{dt}\begin{pmatrix} m_1^x\\ m_1^y\\ m_2^x\\ m_2^y\end{pmatrix} = \begin{pmatrix} 0 & -\omega_E-\omega_K & 0 & -\omega_E\\ \omega_E+\omega_K & 0 & \omega_E & 0\\ 0 & \omega_E & 0 & \omega_E+\omega_K\\ -\omega_E & 0 & -\omega_E-\omega_K & 0\end{pmatrix}\begin{pmatrix} m_1^x\\ m_1^y\\ m_2^x\\ m_2^y\end{pmatrix} + \rho\begin{pmatrix} \beta & -1\\ 1 & \beta\\ -\beta & -1\\ 1 & -\beta\end{pmatrix}\begin{pmatrix} j_x\\ j_y\end{pmatrix}. \qquad \text{(A4)}$$

Given that the presumed solutions and the applied currents have a form $\sim e^{-i\omega t}$, Eq. (5) can be obtained from Eq. (A4) by computing the inverse of matrix.

APPENDIX B: STEADY-STATE LINEAR MODES IN FMS DRIVEN BY SOTS

The ILLG equation of FMs driven by SOTs reads

$$\frac{d\mathbf{m}}{dt} = \mathbf{m}\times\frac{d\mathcal{E}}{d\mathbf{m}} + \alpha\mathbf{m}\times\frac{d\mathbf{m}}{dt} + \eta\mathbf{m}\times\frac{d^2\mathbf{m}}{dt^2} + \boldsymbol{\tau}, \qquad \text{(B1)}$$

where $\mathbf{m}$ is the unit vector of magnetization. The magnetic energy arises from perpendicular magnetocrystalline anisotropy and the demagnetizing field (within the local approximation), and in frequency units, it is given by

$$\mathcal{E} = \omega_K(\mathbf{m}\cdot\mathbf{e}_z)^2, \qquad \text{(B2)}$$

where $\omega_K = \gamma_0 H_K$, with H_K being effective anisotropy field defined by $H_K = 2K_u/M_s - \mu_0 M_s$, with K_u being the magnetocrystalline anisotropy constant, μ_0 the vacuum susceptibility, and M_s the saturation magnetization. The SOTs $\boldsymbol{\tau}$ read

$$\boldsymbol{\tau} = -\rho\{\mathbf{m}\times[\mathbf{m}\times(\mathbf{e}_z\times\mathbf{j}_e)] + \beta\mathbf{m}\times(\mathbf{e}_z\times\mathbf{j}_e)\}, \qquad \text{(B3)}$$

where ρ, β, and $\mathbf{j}_e$ are the same as those in Eq. (3).

By the same procedure as Sec. III, the steady-state linear modes are derived as

$$\begin{bmatrix} m_x(t) \\ m_y(t) \end{bmatrix} = \chi \begin{bmatrix} j_x(t) \\ j_y(t) \end{bmatrix}. \tag{B4}$$

In Eq. (B4), the susceptibility reads

$$\chi = \frac{\rho}{\Delta} \begin{pmatrix} \chi_1 & \chi_2 \\ -\chi_2 & \chi_1 \end{pmatrix}, \tag{B5}$$

where $\chi_1 = \Omega + i(\alpha - \beta)\omega$, $\chi_2 = \beta\Omega + i(1 + \alpha\beta)\omega$, and

$$\Delta = \omega^2 + \Omega^2 + i\alpha\omega, \tag{B6}$$

with $\Omega = \omega_K - \eta\omega^2$. Taking the real parts of Eq. (B4), the linear modes can be written explicitly as

$$m_{x(y)} = \mathcal{A}_{x(y)} \cos[\omega t + \phi_{x(y)}]. \tag{B7}$$

In Eq. (B7), the amplitudes are expressed as

$$\mathcal{A}_{x(y)} = \rho \sqrt{\frac{P_1 J_{x(y)}^2 + P_2 J_{y(x)}^2 + P_3 J_x J_y}{\widetilde{\Delta}}}, \tag{B8}$$

where $P_1 = (\alpha - \beta)^2\omega^2 + \Omega^2$, $P_2 = (1 + \alpha\beta)^2\omega^2 + \beta^2\Omega^2$, $P_3 = 2(1 + \beta^2)\Omega\omega$, and

$$\widetilde{\Delta} = [(\Omega + \omega)^2 + \alpha^2\omega^2][(\Omega - \omega)^2 + \alpha^2\omega^2]. \tag{B9}$$

The phases in Eq. (B7) are given by

$$\phi_x = \tan^{-1}(Q_1 J_x + Q_2 J_y, Q_3 J_x + Q_4 J_y), \tag{B10}$$

$$\phi_y = \tan^{-1}(Q_4 J_x + Q_3 J_y, -Q_2 J_x - Q_1 J_y), \tag{B11}$$

where $\tan^{-1}(x, y)$ denotes the two-argument arctangent, which correctly identifies the quadrant of the point (x, y) [51]. The frequency-dependent parameters Q_i are defined as $Q_1 = \Omega[(1 + 2\alpha\beta - \alpha^2)\omega^2 - \Omega^2]$, $Q_2 = \omega[(1 + \alpha^2)(1 + \alpha\beta)\omega^2 - (1 - \alpha\beta)\Omega^2]$, $Q_3 = \omega[(1 + \alpha^2)(\alpha - \beta)\omega^2 + (\alpha + \beta)\Omega^2]$, and $Q_4 = \Omega[(2\alpha - \beta + \alpha^2\beta)\omega^2 + \beta\Omega^2]$. From Eqs. (B10) and (B11), the phase difference between m_x and m_y is calculated as

$$\Delta\phi \equiv \phi_x - \phi_y = \tan^{-1}(X, Y), \tag{B12}$$

where $X = [(\alpha - \beta)(1 + \alpha\beta)\omega^2 + \beta\Omega^2](J_y^2 - J_x^2)$, and $Y = (1 + \beta^2)\{\Omega\omega(J_x^2 + J_y^2) + [(1 + \alpha^2)\omega^2 + \Omega^2]J_x J_y\}$.

APPENDIX C: RESONANT MODES IN FMS DRIVEN BY SOTS

Assuming $\alpha^2 \ll 1$, Eq. (B8) implies that the resonant frequency satisfies

$$\eta\omega^2 \pm \omega - \omega_K = 0. \tag{C1}$$

Without spin inertia ($\eta = 0$), the resonant frequency is $\pm\omega_K$. In the presence of spin inertia, the resonant frequencies of nutation $\pm\omega_n$ and precession $\pm\omega_p$ are given by

$$\omega_{n,p} = \frac{\sqrt{1 + 2\eta\omega_K} \pm 1}{2\eta}. \tag{C2}$$

From Eq. (B8), the heights of the resonant peaks can be derived. Under the approximations $\alpha^2 \ll 1$, $\alpha\beta \ll 1$, and $\beta^2 \ll 1$, the peak heights are approximately equal for the x and y components of magnetization. Corresponding to the nutation and precession, the peak heights are written as

$$\mathcal{H}_n^{\pm} = \rho\frac{\eta}{\alpha}\frac{|J_x \mp J_y|}{\sqrt{1 + 2\eta\omega_K} + 1}, \tag{C3}$$

$$\mathcal{H}_p^{\pm} = \rho\frac{\eta}{\alpha}\frac{|J_x \pm J_y|}{\sqrt{1 + 2\eta\omega_K} - 1}. \tag{C4}$$

Adopting the same approximation and substituting ω into Eq. (B12), the phase differences corresponding to the $\pm\omega_n$

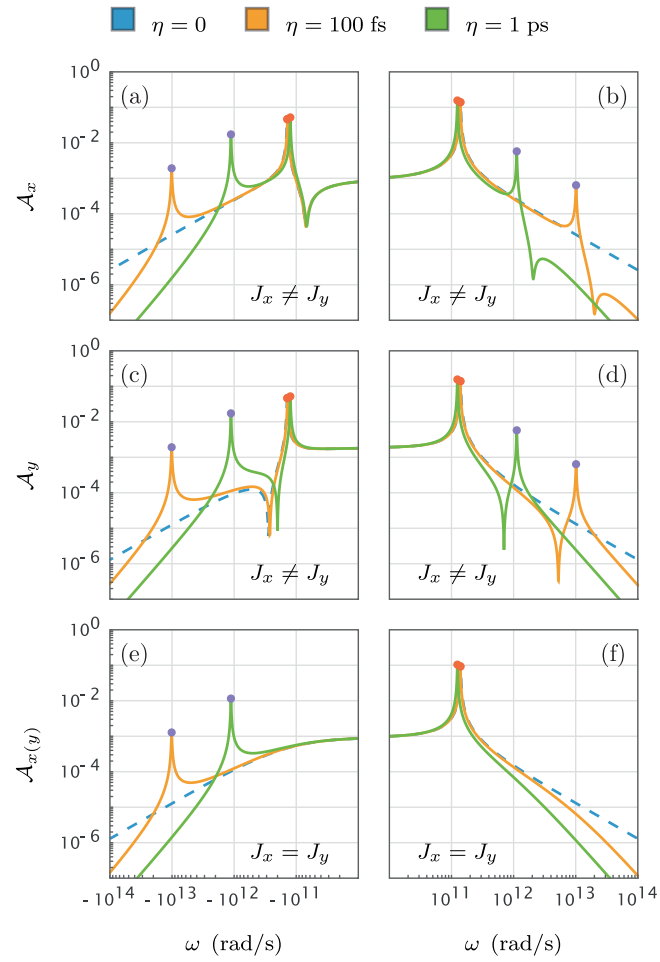


FIG. 7. FM resonant spectra for various values of η. (a)–(d) Under elliptically polarized SOTs ($J_x \neq J_y$), both precessional and nutational FM resonances are excited on the positive- and negative-frequency ranges. (e) and (f) For circular polarization ($J_x = J_y$), the nutational mode is observed at negative frequencies, whereas the precessional mode appears at positive frequencies. Noninertial spectra at $\eta = 0$ are shown with dashed curves. The precessional resonance is shifted by finite spin inertia ($\eta > 0$), and additional nutational resonances are induced (solid curves). Peaks labeled with red (purple) points correspond to precessional (nutational) resonances. To enhance visibility, both axes are shown on a logarithmic scale, and low-frequency regions are omitted. All spectra are calculated from Eq. (B8) using the following parameters: $\omega_K = 0.14$ THz, $\alpha = 0.01$, $\beta = 0.02$, $\rho \approx 0.13\,\mathrm{Hz/(A/m^2)}$; in (a)–(d), $J_x = 1\,\mathrm{GA/m^2}$, $J_y = 2\,\mathrm{GA/m^2}$; in (e) and (f), $J_x = J_y = 1\,\mathrm{GA/m^2}$. For comparison with AFMs, the values of ω_K and ρ are chosen to match those in Fig. 2.

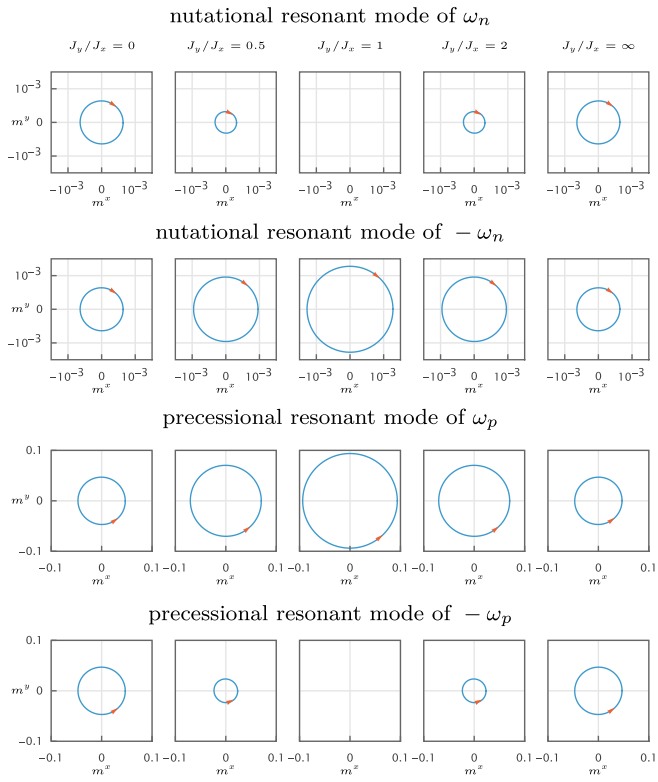


FIG. 8. Polarization and handedness of resonant modes for various ratios J_y/J_x. The inertial relaxation time is set to $\eta = 100$ fs. In each panel, the horizontal and vertical axes represent the m_x and m_y components, respectively. The curves depict the trajectories of the magnetization vector, and the arrows indicate the sense of rotation. In the panels in columns 1–3, $J_x = 1\,\mathrm{GA/m^2}$, and J_y is calculated by the ratio J_y/J_x. In the panels in columns 4–5, $J_y = 1\,\mathrm{GA/m^2}$, and J_x is calculated by the ratio.

and $\pm\omega_p$ resonant modes are given by

$$\Delta\phi_n^{\pm} = \tan^{-1}\left[\alpha\left(J_y^2 - J_x^2\right), \mp(J_x \mp J_y)^2\right], \tag{C5}$$

$$\Delta\phi_p^{\pm} = \tan^{-1}\left[\alpha\left(J_y^2 - J_x^2\right), \pm(J_x \pm J_y)^2\right]. \tag{C6}$$

Equations (C3) and (C4) imply that, for the circularly polarized SOTs ($J_x = J_y$), the nutational mode at ω_n and the precessional mode at $-\omega_p$ are nearly suppressed, as shown in Figs. 7(e) and 7(f). Meanwhile, Eqs. (C5) and (C6) indicate that the phase differences corresponding to the $-\omega_n$ and ω_p resonances are both 90°. Consequently, one finds $-\omega_n \sin\Delta\phi_n^- < 0$ and $\omega_p \sin\Delta\phi_p^+ > 0$, indicating that only the lefthanded nutational mode and righthanded precessional mode are excited by circularly polarized SOTs. This is also illustrated in the third column of Fig. 8. These results qualitatively agree with Ref. [25], where a circularly polarized oscillating magnetic field was used to drive the system.

However, for elliptically polarized SOTs ($J_x \neq J_y$), all resonant modes—both at positive and negative frequencies—can be excited, as shown in Figs. 7(a)–7(d). Moreover, all modes are nearly circularly polarized. For nutational resonances, the phase differences satisfy $180° < \Delta\phi_n^+ < 360°$ and $0° < \Delta\phi_n^- < 180°$, leading to $\pm\omega_n \sin\Delta\phi_n^{\pm} < 0$. Therefore, both the positive- and negative-frequency nutational modes (first and third rows of Fig. 8, respectively) are lefthanded. Similarly, for precessional resonances, one has $0° < \Delta\phi_p^+ < 180°$ and $180° < \Delta\phi_p^- < 360°$, which results in $\pm\omega_p \sin\Delta\phi_p^{\pm} > 0$. Consequently, both the positive- and negative-frequency precessional modes (second and fourth rows of Fig. 8) are righthanded. In summary, regardless of whether the SOT is righthanded or lefthanded, nutational resonant modes in FMs are always lefthanded, while precessional resonant modes are always righthanded.

[1] R. Mondal, L. Rózsa, M. Farle, P. M. Oppeneer, U. Nowak, and M. Cherkasskii, Inertial effects in ultrafast spin dynamics, J. Magn. Magn. Mater. **579**, 170830 (2023).

[2] S. Bhattacharjee, L. Nordström, and J. Fransson, Atomistic spin dynamic method with both damping and moment of inertia effects included from first principles, Phys. Rev. Lett. **108**, 057204 (2012).

[3] R. Mondal, M. Berritta, and P. M. Oppeneer, Generalisation of Gilbert damping and magnetic inertia parameter as a series of higher-order relativistic terms, J. Phys.: Condens. Matter **30**, 265801 (2018).

[4] M. G. Quarenta, M. Tharmalingam, T. Ludwig, H. Y. Yuan, L. Karwacki, R. C. Verstraten, and R. A. Duine, Bath-induced spin inertia, Phys. Rev. Lett. **133**, 136701 (2024).

[5] J. Anders, C. R. J. Sait, and S. A. R. Horsley, Quantum Brownian motion for magnets, New J. Phys. **24**, 033020 (2022).

[6] T. Kikuchi and G. Tatara, Spin dynamics with inertia in metallic ferromagnets, Phys. Rev. B **92**, 184410 (2015).

[7] S. Giordano and P.-M. Déjardin, Derivation of magnetic inertial effects from the classical mechanics of a circular current loop, Phys. Rev. B **102**, 214406 (2020).

[8] J.-E. Wegrowe and M.-C. Ciornei, Magnetization dynamics, gyromagnetic relation, and inertial effects, Am. J. Phys. **80**, 607 (2012).

[9] M.-C. Ciornei, J. M. Rubí, and J.-E. Wegrowe, Magnetization dynamics in the inertial regime: Nutation predicted at short time scales, Phys. Rev. B **83**, 020410(R) (2011).

[10] D. Böttcher and J. Henk, Significance of nutation in magnetization dynamics of nanostructures, Phys. Rev. B **86**, 020404(R) (2012).

[11] S. V. Titov, W. T. Coffey, Y. P. Kalmykov, and M. Zarifakis, Deterministic inertial dynamics of the magnetization of nanoscale ferromagnets, Phys. Rev. B **103**, 214444 (2021).

[12] S. V. Titov, Y. P. Kalmykov, K. D. Kazarinov, M. A. Cherkasskii, and A. S. Titov, Inertial magnetization dynamics in ferromagnetic nanoparticles near saturation, J. Commun. Technol. Electron. **68**, 559 (2023).

[13] Y. Li, A.-L. Barra, S. Auffret, U. Ebels, and W. E. Bailey, Inertial terms to magnetization dynamics in ferromagnetic thin films, Phys. Rev. B **92**, 140413(R) (2015).

[14] K. Neeraj, N. Awari, S. Kovalev, D. Polley, N. Zhou Hagström, S. S. P. K. Arekapudi, A. Semisalova, K. Lenz, B. Green, J.-C.

Deinert *et al.*, Inertial spin dynamics in ferromagnets, Nat. Phys. **17**, 245 (2021).

[15] V. Unikandanunni, R. Medapalli, M. Asa, E. Albisetti, D. Petti, R. Bertacco, E. E. Fullerton, and S. Bonetti, Inertial spin dynamics in epitaxial cobalt films, Phys. Rev. Lett. **129**, 237201 (2022).

[16] A. De, J. Schlegel, A. Lentfert, L. Scheuer, B. Stadtmüller, P. Pirro, G. von Freymann, U. Nowak, and M. Aeschlimann, Magnetic nutation: Transient separation of magnetization from its angular momentum, Phys. Rev. B **111**, 014432 (2025).

[17] P.-B. He, Large-amplitude and widely tunable self-oscillations enabled by the inertial effect in uniaxial antiferromagnets driven by spin-orbit torques, Phys. Rev. B **108**, 184418 (2023).

[18] P.-B. He, Influence of the magnetic inertia on the self-oscillation in spin-orbit torque-driven tripartite antiferromagnets with a 120° rotation symmetry, Phys. Rev. B **110**, 064411 (2024).

[19] R. Rodriguez, M. Cherkasskii, R. Jiang, R. Mondal, A. Etesamirad, A. Tossounian, B. A. Ivanov, and I. Barsukov, Spin inertia and auto-oscillations in ferromagnets, Phys. Rev. Lett. **132**, 246701 (2024).

[20] E. Olive, Y. Lansac, and J.-E. Wegrowe, Beyond ferromagnetic resonance: The inertial regime of the magnetization, Appl. Phys. Lett. **100**, 192407 (2012).

[21] E. Olive, Y. Lansac, M. Meyer, M. Hayoun, and J.-E. Wegrowe, Deviation from the Landau-Lifshitz-Gilbert equation in the inertial regime of the magnetization, J. Appl. Phys. **117**, 213904 (2015).

[22] M. Cherkasskii, M. Farle, and A. Semisalova, Nutation resonance in ferromagnets, Phys. Rev. B **102**, 184432 (2020).

[23] R. Mondal, S. Großenbach, L. Rózsa, and U. Nowak, Nutation in antiferromagnetic resonance, Phys. Rev. B **103**, 104404 (2021).

[24] R. Mondal and P. M. Oppeneer, Influence of intersublattice coupling on the terahertz nutation spin dynamics in antiferromagnets, Phys. Rev. B **104**, 104405 (2021).

[25] R. Mondal and A. Kamra, Spin pumping at terahertz nutation resonances, Phys. Rev. B **104**, 214426 (2021).

[26] R. Mondal, Theroy of magnetic inertial dynamics in two-sublattice ferromagnets, J. Phys.: Condens. Matter **33**, 275804 (2021).

[27] S. V. Titov, W. J. Dowling, and Y. P. Kalmykov, Ferromagnetic and nutation resonance frequencies of nanomagnets with various magnetocrystalline anisotropies, J. Appl. Phys. **131**, 193901 (2022).

[28] M. Cherkasskii, I. Barsukov, R. Mondal, M. Farle, and A. Semisalova, Theory of inertial spin dynamics in anisotropic ferromagnets, Phys. Rev. B **106**, 054428 (2022).

[29] S. Ghosh, M. Cherkasskii, I. Barsukov, and R. Mondal, Theory of tensorial magnetic inertia in terahertz spin dynamics, Phys. Rev. B **110**, 174430 (2024).

[30] R. Cheng, M. W. Daniels, J.-G. Zhu, and D. Xiao, Antiferromagnetic spin wave field-effect transistor, Sci. Rep. **6**, 24223 (2016).

[31] T. Yu, C. Cai, and G. E. W. Bauer, Chirality enables thermal magnon transistors, Sci. China Phys. Mech. Astron. **67**, 247511 (2024).

[32] W. Yu, J. Lan, and J. Xiao, Magnetic logic gate based on polarized spin waves, Phys. Rev. Appl. **13**, 024055 (2020).

[33] C. Jia, M. Chen, A. F. Schäffer, and J. Berakdar, Chiral logic computing with twisted antiferromagnetic magnon modes, npj Comput. Mater. **7**, 101 (2021).

[34] A. A. Tulapurkar, Y. Suzuki, A. Fukushima, H. Kubota, H. Maehara, K. Tsunekawa, D. D. Djayaprawira, N. Watanabe, and S. Yuasa, Spin-torque diode effect in magnetic tunnel junctions, Nature (London) **438**, 339 (2005).

[35] J. C. Sankey, P. M. Braganca, A. G. F. Garcia, I. N. Krivorotov, R. A. Buhrman, and D. C. Ralph, Spin-transfer-driven ferromagnetic resonance of individual nanomagnets, Phys. Rev. Lett. **96**, 227601 (2006).

[36] H. Xi, Y. Shi, and K.-Z. Gao, Spin-current effect on ferromagnetic resonance in patterned magnetic thin film structures, J. Appl. Phys. **97**, 033904 (2005).

[37] J. N. Kupferschmidt, S. Adam, and P. W. Brouwer, Theory of the spin-torque-driven ferromagnetic resonance in a ferromagnet/normal-metal/ferromagnet structure, Phys. Rev. B **74**, 134416 (2006).

[38] A. A. Kovalev, G. E. W. Bauer, and A. Brataas, Current-driven ferromagnetic resonance, mechanical torques, and rotary motion in magnetic nanostructures, Phys. Rev. B **75**, 014430 (2007).

[39] P.-B. He, Z.-D. Li, A.-L. Pan, Q. Wan, Q.-L. Zhang, R.-X. Wang, Y.-G. Wang, W.-M. Liu, and B.-S. Zou, Theory of ferromagnetic resonance in magnetic trilayers with a tilted spin polarizer, Phys. Rev. B **78**, 054420 (2008).

[40] L. Liu, T. Moriyama, D. C. Ralph, and R. A. Buhrman, Spin-torque ferromagnetic resonance induced by the spin Hall effect, Phys. Rev. Lett. **106**, 036601 (2011).

[41] K. Kondou, H. Sukegawa, S. Mitani, K. Tsukagoshi, and S. Kasai, Evaluation of spin Hall angle and spin diffusion length by using spin current-induced ferromagnetic resonance, Appl. Phys. Express **5**, 073002 (2012).

[42] V. Sluka, Antiferromagnetic resonance excited by oscillating electric currents, Phys. Rev. B **96**, 214412 (2017).

[43] C. Sun, H. Yang, and M. B. A. Jalil, Ferrimagnetic resonance induced by the spin Hall effect, Phys. Rev. B **102**, 134420 (2020).

[44] D. Thonig, O. Eriksson, and M. Pereiro, Magnetic moment of inertia within the torque-torque correlation model, Sci. Rep. **7**, 931 (2017).

[45] A. Manchon, J. Železný, I. M. Miron, T. Jungwirth, J. Sinova, A. Thiaville, K. Garello, and P. Gambardella, Current-induced spin-orbit torques in ferromagnetic and antiferromagnetic systems, Rev. Mod. Phys. **91**, 035004 (2019).

[46] L. Zhu, D. C. Ralph, and R. A. Buhrman, Highly efficient spin-current generation by the spin Hall effect in $Au_{1-x}Pt_x$, Phys. Rev. Appl. **10**, 031001(R) (2018).

[47] C.-F. Pai, Y. Ou, L. H. Vilela-Leão, D. C. Ralph, and R. A. Buhrman, Dependence of the efficiency of spin Hall torque on the transparency of Pt/ferromagnetic layer interfaces, Phys. Rev. B **92**, 064426 (2015).

[48] Z. Wang, H. Cheng, K. Shi, Y. Liu, J. Qiao, D. Zhu, W. Cai, X. Zhang, S. Eimer, D. Zhu *et al.*, Modulation of field-like spin orbit torque in heavy metal/ferromagnet heterostructures, Nanoscale **12**, 15246 (2020).

[49] J. Bouaziz, M. dos Santos Dias, F. S. M. Guimarães, and S. Lounis, Spin dynamics of 3*d* and 4*d* impurities embedded in

prototypical topological insulators, Phys. Rev. Mater. **3**, 054201 (2019).

[50] D. D. Stancil and A. Prabhakar, *Spin Waves: Theory and Applications* (Springer, New York, 2009).

[51] W. Research, Arctan, Wolfram language function (1988) (updated 2021).

[52] P. Vaidya, S. A. Morley, J. V. Tol, Y. Liu, R. Cheng, A. Brataas, D. Lederman, and E. D. Barco, Subterahertz spin pumping from an insulating antiferromagnet, Science **368**, 160 (2020).

[53] S. M. Rezende, A. Azevedo, and R. L. Rodríguez-Suárez, Introduction to antiferromagnetic magnons, J. Appl. Phys. **126**, 151101 (2019).

[54] Y. Shiota, T. Taniguchi, D. Hayashi, H. Narita, S. Karube, R. Hisatomi, T. Moriyama, and T. Ono, Handedness manipulation of propagating antiferromagnetic magnons, Nat. Commun. **15**, 9750 (2024).

[55] X. Chen, C. Zheng, Y. Zhang, S. Zhou, Y. Liu, and Z. Zhang, Identification and manipulation of spin wave polarizations in perpendicularly magnetized synthetic antiferromagnets, New J. Phys. **23**, 113029 (2021).

[56] I. Boventer, H. T. Simensen, A. Anane, M. Kläui, A. Brataas, and R. Lebrun, Room-temperature antiferromagnetic resonance and inverse spin-Hall voltage in canted antiferromagnets, Phys. Rev. Lett. **126**, 187201 (2021).